ORIGINAL ARTICLE

Somatic Loss-of-Function *PIK3R1* and Activating Non-hotspot *PIK3CA* Mutations Associated with Capillary Malformation with Dilated Veins (CMDV)

Martina De Bortoli[1], Angela Queisser[1], Van Cuong Pham[2], Anne Dompmartin[3], Raphaël Helaers[1], Simon Boutry[1,4], Cathy Claus[5], An-Katrien De Roo[5,6,7], Frank Hammer[8], Pascal Brouillard[1], Salim Abdelilah-Seyfried[2], Laurence M. Boon[1,5] and Miikka Vikkula[1,5,9]

Common capillary malformations are red vascular skin lesions, most commonly associated with somatic activating *GNAQ* or *GNA11* mutations. We focused on capillary malformations lacking such a mutation to identify previously unreported genetic causes. We used targeted next-generation sequencing on 82 lesions. Bioinformatic analysis allowed the identification of 9 somatic pathogenic variants in *PIK3R1* and *PIK3CA*, encoding for the regulatory and catalytic subunits of phosphoinositide 3-kinase, respectively. Recharacterization of these lesions unraveled a common phenotype: a pale capillary malformation associated with visible dilated veins. Primary endothelial cells from 2 *PIK3R1*-mutated lesions were isolated, and PI3k-Akt-mTOR and RAS−RAF−MAPK signaling were assessed by western blot. This unveiled an abnormal increase in Akt phosphorylation, effectively reduced by PI3K pathway inhibitors, such as mTOR, Akt, and PIK3CA inhibitors. The effects of mutant *PIK3R1* were further studied using zebrafish embryos. Endothelium-specific expression of *PIK3R1* mutants resulted in abnormal development of the posterior capillary−venous plexus. In summary, capillary malformation associated with visible dilated veins emerges as a clinical entity associated with somatic pathogenic variants in *PIK3R1* or *PIK3CA* (nonhotspot). Our findings suggest that the activated Akt signaling can be effectively reversed by PI3K pathway inhibitors. In addition, the proposed zebrafish model holds promise as a valuable tool for future drug screening aimed at developing patient-tailored treatments.

Keywords: Endothelial, NGS, PI3K signaling, Somatic, Zebrafish

Journal of Investigative Dermatology (2024) **144,** 2066−2077; doi:10.1016/j.jid.2024.01.033

INTRODUCTION

Capillary malformations (CMs), commonly known as port-wine stains, are usually unifocal lesions, affecting mainly the skin or mucosa in localized areas. CMs usually appear sporadically as red or purple flat macules. They are the most common cutaneous vascular malformation, affecting around 3 in 1000 newborns (Uebelhoer et al, 2012; Walton et al, 1976). Most of the sporadic cases (around 90%) of common CMs have been associated with an activating somatic mutation in either the *GNAQ* or *GNA11* genes (Couto et al, 2016; Nakashima et al, 2014). Less common capillary phenotypes also exist: (i) more extensive CM, such as CM with overgrowth or diffuse CM with proportionate overgrowth; (ii) multifocal CMs, such as in capillary malformation arteriovenous malformation (arteriovenous malformation−associated CM types 1 and 2; and (iii) combined lesions, such as capillaro−lymphatico−venous malformation (CLVM) and capillary−venous malformations (Uihlein et al, 2013) with or without overgrowth. Some CM with overgrowth and diffuse CM with proportionate overgrowth have been shown to associate with somatic *GNAQ* and *PIK3CA* non-hotspot mutations, respectively (Goss et al, 2020; Jordan et al, 2020), whereas arteriovenous malformation−associated CM types 1 and 2 are associated with germline *RASA1* and *EPHB4* mutations (Amyere et al, 2017; Eerola et al, 2003). Many of the patients with

[1]*Laboratory of Human Molecular Genetics, de Duve Institute, UCLouvain, Brussels, Belgium;* [2]*Institute of Biochemistry and Biology, University of Potsdam, Potsdam, Germany;* [3]*Department of Dermatology, VASCERN VASCA European Reference Center, Université de Caen Basse Normandie, Caen, France;* [4]*Interuniversity Institute of Bioinformatics in Brussels, Université Libre de Bruxelles-Vrije Universiteit Brussel, Brussels, Belgium;* [5]*Center for Vascular Anomalies, Division of Plastic Surgery, VASCERN VASCA European Reference Center, Cliniques Universitaires Saint Luc, UCLouvain, Brussels, Belgium;* [6]*Service d'anatomopathologie, VASCERN VASCA European Reference Center, Cliniques Universitaires Saint Luc, UCLouvain, Brussels, Belgium;* [7]*Institute of Experimental and Clinical Research, UCLouvain, Brussels, Belgium;* [8]*Department of Medical Imaging, VASCERN VASCA European Reference Center, Cliniques Universitaires Saint-Luc, UCLouvain, Brussels, Belgium; and* [9]*WELBIO Department, WEL Research Institute, Wavre, Belgium*

Correspondence: Miikka Vikkula, Human Molecular Genetics, de Duve Institute, University of Louvain, Avenue Hippocrate 74 (+5), bte B1.74.06, Brussels B-1200, Belgium. E-mail: miikka.vikkula@uclouvain.be

Abbreviations: Akt, protein kinase B; CLVM, capillaro−lymphatico−venous malformation; CM, capillary malformation; CMDV, capillary malformation with visible dilated veins; CV, caudal vein; DA, dorsal aorta; EC, endothelial cell; HUVEC, human umbilical vein endothelial cell; pAkt, phosphorylated protein kinase B; pERK, phosphorylated extracellular signal−regulated kinase; PI3K, phosphoinositide 3-kinase; WT, wild type

Received 18 September 2023; revised 25 January 2024; accepted 27 January 2024; accepted manuscript published online 29 February 2024; corrected proof published online 25 March 2024

combined lesions bear a somatic activating *PIK3CA* hotspot mutation (Brouillard et al, 2021; Keppler-Noreuil et al, 2016). Nonetheless, numerous CM lesions remain unsolved, without detection of such a mutation.

To date, gold-standard treatments for vascular malformations include laser, sclerotherapy, embolization, and surgical resection. Since the discovery of the underlying signaling pathways that are shared with cancers, oncology drugs have been tested in preclinical models of vascular malformations and also in clinical trials (Adams et al, 2016; Boon et al, 2022; Boscolo et al, 2015; Harbers et al, 2023; Queisser et al, 2021; Seront et al, 2023). These drugs have demonstrated their effectiveness in patients with vascular anomalies, and they will likely be selected on the basis of patients' genotypes. Therefore, it has become crucial to identify all the genes and mutations that can lead to vascular anomalies.

We have sequenced DNA from resected lesions and from patient-derived endothelial cells (ECs) from a cohort of individuals affected by sporadically occurring CM. No mutation in *GNAQ* or *GNA11* had been detected, and other genes were analyzed. We describe somatic mutations in 2 genes belonging to the phosphoinositide 3-kinase (PI3K)/protein kinase B (Akt)/mTOR pathway, observe activation of this pathway and their response to drug treatment in isolated ECs, and show a zebrafish model we generated for one of the genes. Our clinical re-evaluation of the patients revealed lesions with characteristics that differ from those of common CMs: a pale CM with visible dilated veins (CMDV). This entity has been previously reported in the literature as capillary-venous malformation (Uihlein et al, 2013). In this study, we propose a diagnostic term that more precisely describes the clinical characteristics since we do not observe a proper venous malformation in these lesions.

RESULTS

PIK3R1 and *PIK3CA* somatic variants found in 9 patients

We identified *PIK3R1* (NM_181523.2) or *PIK3CA* (NM_006218.2) somatic variants in the lesions resected from 9 individuals (Table 1). Four were distinct variants in *PIK3R1*, and 3 were in *PIK3CA*, from 5 and 4 patients, respectively (Figure 1 and Table 1). All the identified variants in *PIK3R1* and *PIK3CA* are predicted to be damaging by at least 11 prediction algorithms and reported in the COSMIC (Catalogue Of Somatic Mutations In Cancer) database for cancer somatic mutations. Three of the 4 *PIK3R1* variants (G376R, N564D, and L573P) are among the 20 most recurrent *PIK3R1* variants on a total of 1663 observed in cancers (Table 1), whereas the 3 variants in *PIK3CA* are not the canonical hotspots (Figure 1b, in grey). The variant allele frequency ranged from 3% to 18%, reflecting somatic etiology (Table 1). The 4 *PIK3R1* variants were missense changes located in the nSH2 (n = 1) or the PI3K_p85_iSH2 (n = 3, accounting for 4 patients) domains of the p85 protein (Figure 1a). These domains interact with the catalytic p110 subunits of PI3K. The 3 distinct missense changes in *PIK3CA* were located in the C2 domain (n = 2, accounting for 3 patients) or in the PI3K catalytic domain of the p110 protein (n = 1) (Figure 1b). To date, on the total of 82 screened individuals, 61 still remain unsolved.

Patients harboring *PIK3CA* and *PIK3R1* variants have distinct clinical entity

After identification of the genetic variants, the clinical re-evaluation noted similarities between the lesions. The lesion size varied from small patches to more extensive ones. They manifested as red to dark–red lesions at birth, with indistinct borders, becoming paler and more purple colored over time (Figure 2c). They also had visible dilated veins along with the CM, irrespective of the body part they were localized in (Figure 2).

Seven of the 9 patients had a lesion localized on the lower extremities (patients 1–6 and 9) (Figure 2). Patient 7 had a lesion on the upper extremity (from hand to axilla), whereas patient 8 had a lesion on the right lower flank only. Two of the patients with lower extremity lesions had an extensive CMDV: patient 9 had a lesion on the entire left lower extremity with varicose veins in the genitalia, and patient 2 had

Table 1. Characteristics of *PIK3CA* and *PIK3R1* Identified Variants

Individual	Gene Symbol	NT Change	AA Change	VAF	Consensus Prediction	Protein Domain	DNA Source	COSMIC ID
Tissue 1	*PIK3CA*	c.1133G>A	Cys378Tyr	7%	16	PI3K_C2	RNAlater	COSV55952006 (4×)
Tissue 2	*PIK3CA*	c.1357G>A	Glu453Lys	6%	16	PI3K_C2	RNAlater	COSV55874585 (82×)
Tissue 3	*PIK3CA*	c.1357G>A	Glu453Lys	3%	16	PI3K_C2	RNAlater	COSV55874585 (82×)
Tissue 4	*PIK3CA*	c.3129G>T	Met1043Ile	5%	11	PI3K_catalytic	RNAlater	COSV55878974 (85×)
Tissue 5	*PIK3R1*	c.1126G>A	Gly376Arg	8%	18	nSH2	Frozen Tissue	COSV57123316 (31×)
Tissue 6	*PIK3R1*	c.1690A>G	Asn564Asp	3%	13	PI3K_p85_iSH2	Frozen Tissue	COSV57124003 (49×)
Tissue 7[1]	*PIK3R1*	c.1690A>G	Asn564Asp	11%	13	PI3K_p85_iSH2	Frozen Tissue	COSV57124003 (49×)
Tissue 8	*PIK3R1*	c.1709T>C	Leu570Pro	4%	16	PI3K_p85_iSH2	RNAlater	COSV57123228 (3×)
Tissue 9[2]	*PIK3R1*	c.1718T>C	Leu573Pro	18%	16	PI3K_p85_iSH2	Frozen Tissue	COSV57124674 (11×)
EC-N564D[1]	*PIK3R1*	c.1690A>G	Asn564Asp	50%	13	PI3K_p85_iSH2	Primary EC	COSV57124003 (49×)
EC-L573P[2]	*PIK3R1*	c.1718T>C	Leu573Pro	50%	16	PI3K_p85_iSH2	Primary EC	COSV57124674 (11×)

Abbreviations: AA, amino acid; COSMIC, Catalogue Of Somatic Mutations In Cancer; EC, endothelial cell; ID, identification; NT, nucleotide; VAF, variant allele frequency.
Consensus prediction is defined as the number of algorithms predicting the variant to be damaging.
[1]Samples from the same individual.
[2]Samples from the same individual.

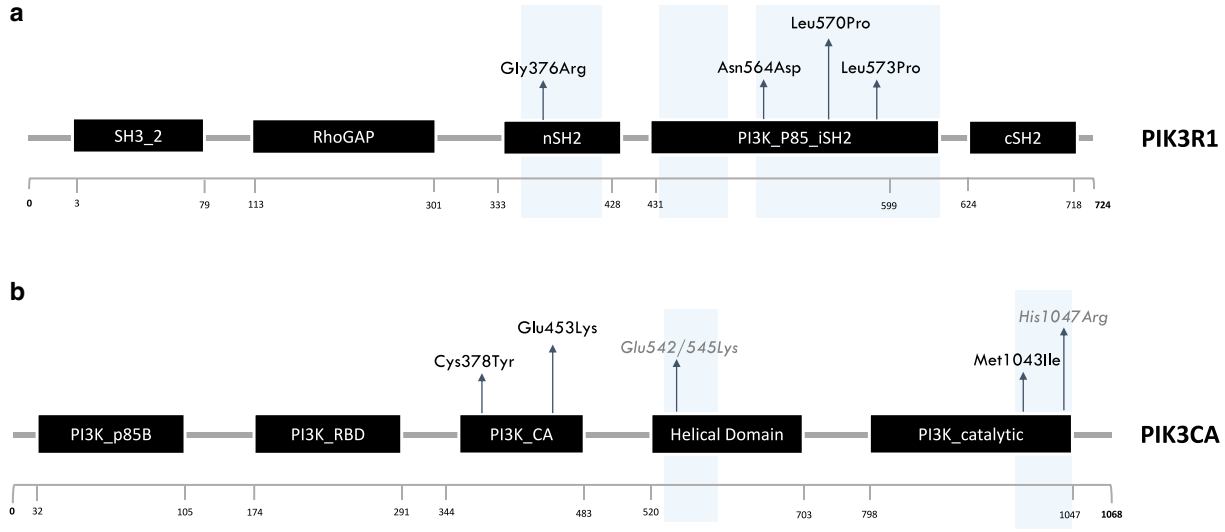

Figure 1. PIK3CA and PIK3R1 protein structures and distribution of identified variants. **(a)** *PIK3R1* protein (p85) and its functional domains. Variants localized in the nSH2 domain (n = 1) and in the PI3K_P85_iSH2 domain (n = 3). L570P and L573P variants are predicted to be pathogenic but lack experimental validation. **(b)** *PIK3CA* (p110) and its functional domains. Variants reported in black localized in the Ca^{2+}-binding domain (n = 2) and in PI3K catalytic domain (n = 1). Hotspot *PIK3CA* mutations are in grey. Cancer hotspot regions are highlighted in light blue. Ca^{2+}, calcium ion; PI3K, phosphoinositide 3-kinase.

bilateral lesions extending to the lower back. The other lower extremity lesions affected only partially the limb (Figure 2).

Doppler ultrasound and magnetic resonance imaging showed dilation of the superficial, muscular, and sometimes deep veins without aplasia or hypoplasia of the deep venous system or persistent embryonic veins (Figure 2d). D-dimers levels were in the physiological range for all patients, except for individual 2 in whom they were found to be slightly increased during sporadic episodes of pain. Some patients had mild hypotrophy or hypertrophy of soft tissue or bone with larger or smaller girth and/or longer or shorter leg (n = 4) (Table 2). There were no foot or toe anomalies. Patients reported pain at the site of the dilated veins, mostly mild, with episodes of stronger pain (n = 3). Only 1 patient reported functional limitations due to pain (individual 1). None of the patients displayed signs of overgrowth or lymphatic malformations. Treatment of these patients is now limited to pain management, when necessary, and treatment of dilated veins using surgical or sclerotherapeutical approaches.

Patient-derived ECs with *PIK3R1* mutations show activation of PI3K–Akt–mTOR and RAS–RAF–MAPK pathways

Primary ECs derived from surgical resections of 2 *PIK3R1*-positive lesions were isolated from non-ECs. $CD31^+$ cells displayed the cobblestone morphology typically seen for ECs, whereas $CD31^-$ cells appeared more elongated (Figure 3a). The isolated ECs expressed CD31 (in red) and a second EC marker, von Willebrand factor (in green) (Figure 3b).

To confirm the presence of the *PIK3R1* mutation and to define variant allele frequency, DNA of the patient-derived ECs were sequenced by targeted next-generation sequencing. One EC bore the same c.1690A>G (N564D) variant as the corresponding tissue sample (tissue 7) (Tables 1 and 2), whereas the other harbored the same c.1718T>C (L573P) *PIK3R1* variant as the corresponding tissue sample (tissue 9) (Tables 1 and 2). From this point forward, they will be referred to as EC-N564D and EC-L573P, respectively. Both $CD31^+$ cells had a variant allele frequency around 50%. In $CD31^-$ cells, no *PIK3R1* variant was detected.

To assess whether the *PIK3R1* variants could trigger activation of the PI3K–Akt–mTOR or the RAS–RAF–MAPK pathway in the mutant ECs, we measured the levels of phosphorylated Akt (pAkt) and phosphorylated extracellular signal–regulated kinase (pERK). Compared with that in human umbilical vein ECs (HUVECs), Akt phosphorylation was increased in both EC-N564D and EC-L573P cells as well as in control ECs expressing *PIK3CA* hotspot mutation (Figure 4a and b). In addition, EC-N564D cells grown under starved conditions induced higher levels of pAkt than HUVECs (Figure 4a and b). ERK phosphorylation was observed when EC-N564D cells were grown in complete medium as well as in starved conditions (Figure 4c). pERK levels were also higher in EC-L573P cells than in HUVECs (Figure 4d).

PI3K–Akt–mTOR and RAS–RAF–MAPK pathways effectively inhibited in *PIK3R1* mutant ECs

Patient-derived ECs were treated with inhibitors acting at different levels of the PI3K–Akt–mTOR signaling pathway: the mTOR inhibitor rapamycin (sirolimus), the Akt inhibitor MK2206, and the PIK3CA inhibitor BYL719 (alpelisib). Treatment of EC-N564D and EC-L573P resulted in a significant decrease in pAkt (Figure 4a and b). The reduction was particularly striking when MK2206 and BYL719 were used. A decrease in pERK was also observed, but this was limited to the treatment with the PIK3CA inhibitor BYL719 (Figure 4c and d). Of note, the experiments were only performed twice for EC-L573P because the piece of tissue harvested during surgical procedure was small and the number of passages that were obtained for the limited number of ECs was low before they ceased to grow.

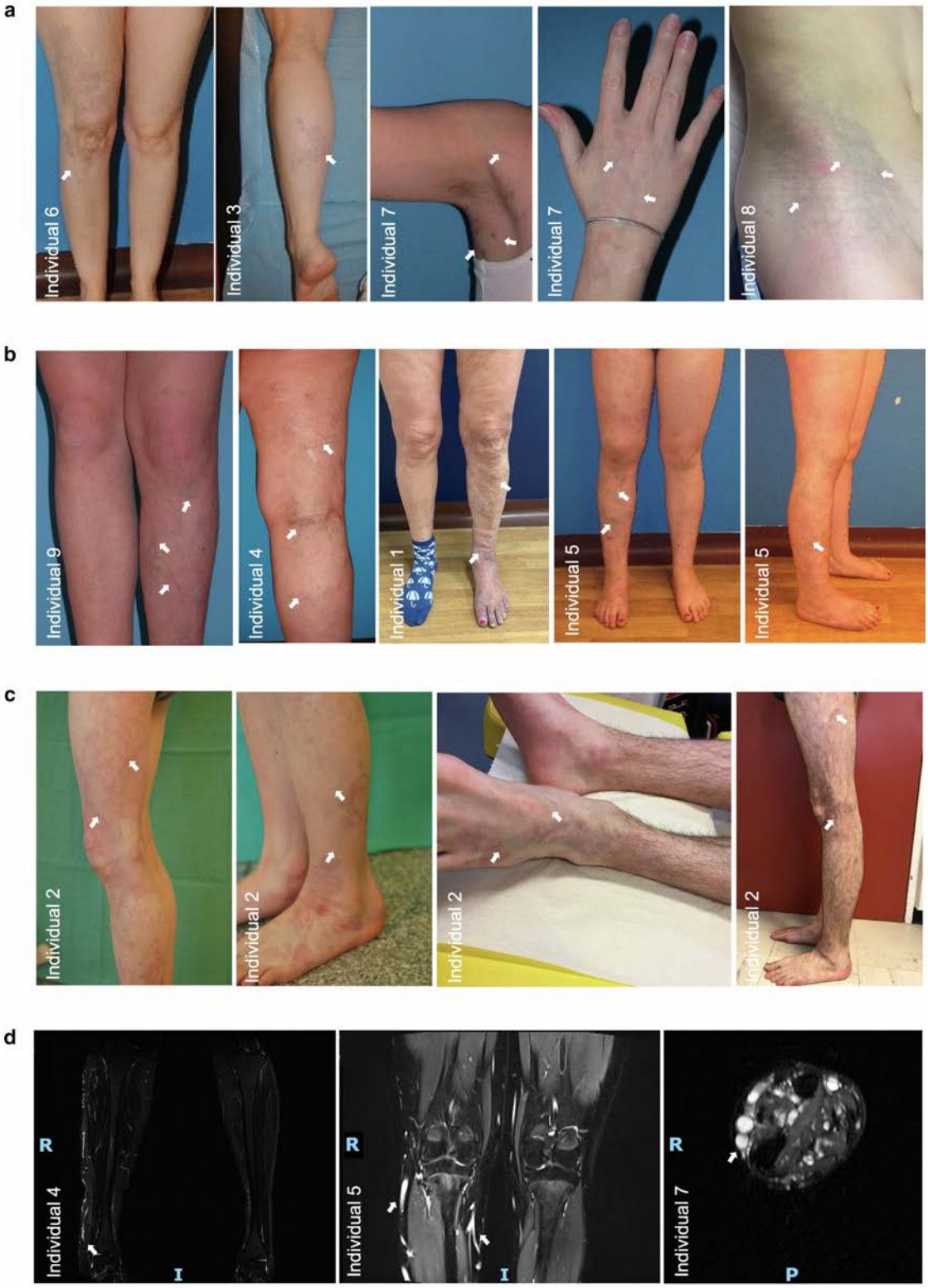

Figure 2. Clinical phenotype of patients with CMDV with PIK3R1 or nonhot post-PIK3CA variants. Patients characterized by localized CMs and dilated veins visible on skin and MRI (white arrows). **(a)** Patients with smaller lesions and less prominent veins. **(b)** Patients with more extensive lesions and strongly prominent veins. **(c)** Progression of lesion in individual 2 from the age 7 to the age of 21 year: veins became more prominent and dilated, and CM turned from reddish to purplish color. **(d)** MRI (fat suppression sequence, 1.5T) of the lower limbs of patients 4, 5, and 7 showing hyperintense slow-flowing blood in dilated veins of the subcutaneous tissues. All subjects or their parent/guardian included in this study consented to publication of the images shown in this figure. CM, capillary malformation; CMDV, capillary malformation with dilated veins; MRI, magnetic resonance imaging.

Table 2. Clinical Characteristic of Patients with *PIK3R1* and *PIK3CA* Variants

Individual	Age at Operation	Sex	Gene	Nucleotide Change	Hypotrophy Limb	Hypertrophy Limb	Pain (VAS/10)	D-Dimers
Tissue 1	55	F	*PIK3CA*	c.1357G>A	Left leg (12 mm length)	Mild (girth)	5 (episodes of 8)	Normal
Tissue 2	17	M	*PIK3CA*	c.1357G>A	Hypoplasia	—	7 in infancy	Normal (up to 605 ng/ml when in pain)
Tissue 3	43	F	*PIK3CA*	c.3129G>T	—	—	3	Normal
Tissue 4	41	F	*PIK3CA*	c.1133G>A	—	Mild left leg (length 9 mm; thigh girth 6 cm)	6 (episodes of 9)	Normal
Tissue 5	14	F	*PIK3R1*	c.1126G>A	—	Mild (girth)	3–4	Normal
Tissue 6	39	F	*PIK3R1*	c.1690A>G	—	—	5	Normal
Tissue 7	26	F	*PIK3R1*	c.1690A>G	—	—	4–5	N/A
Tissue 8	10	M	*PIK3R1*	c.1709T>C	—	—	5 in infancy	Normal
Tissue 9	24	F	*PIK3R1*	c.1718T>C	Left leg (13 mm length)	—	4–5	Normal

Abbreviations: F, female; M, male; N/A, not available; VAS, Visual Analog Scale.

Endothelium-specific expression of mutant *PIK3R1* in zebrafish embryos leads to malformations in the capillary–venous network

To further assess the effects of the CMDV-PIK3R1 variants, we generated zebrafish models. We first performed a knockdown experiment in Tg*(fli1a:Gal4FF^{ubs3};UAS:RFP)* embryos, by injecting a spliced *Pik3r1* morpholino at one-cell stage, to evaluate the overall effect of *Pik3r1* loss. Compared with uninjected embryos, the diameter of the caudal vein (CV) was significantly increased (Supplementary Figure S1a).

In addition, we performed endothelium-specific mosaic overexpression of the wild type (WT)/mutant human *PIK3R1* transgene in zebrafish. Upon overexpression of *PIK3R1*^{N564D}, *PIK3R1*^{L570P}, and *PIK3R1*^{L573P} mutations in these embryos, the capillary plexus appeared mostly disorganized, showing an irregular, compressed morphology with indistinguishable individual vessels rather than an organized pattern of small, connected vessels (Figure 5a–f). This phenotype was more objectively measured by spatial analysis of the vascular area by calculating the ratio between the intravascular and intervascular spaces within the capillary bed, which corroborated our initial visual observation (Figure 5g).

Moreover, overexpression of *PIK3R1*^{L570P} and *PIK3R1*^{L573P} but not of *PIK3R1*^{N564D} led to enlargement of the CV diameter (Figure 5a–f and h). Neither morphants nor mutant fish exhibited any indication of developmental delay (Supplementary Figure S2). Embryos in which the CV was not readily distinguishable were omitted from the analysis. This was more frequent for mutant embryos than for control or WT embryos (Supplementary Table S1). This trend is particularly pronounced in *PIK3R1*^{N564D}, *PIK3R1*$^{N564D+pik3r1Mo}$, and *PIK3R1*^{L573P} mutants, in which the percentage of discarded embryos reached 42.8, 33.33, and 30.7%, respectively (Supplementary Table S1).

To assess whether WT or mutant *PIK3R1* could rescue the phenotype induced by the morpholino, knocked down embryos were injected along with the corresponding plasmids. We found that the vascular phenotype was solely attributable to the gene knockdown. In fact, neither the mutant nor the WT *PIK3R1* mosaic re-expression had the capacity to rescue the CV phenotype, nor did it induce any additional phenotypic changes (Supplementary Figure S1b–d). No variant-specific additional phenotypes were observed. The rate of plasmid integration was estimated by counting the number of EGFP^{+} ECs in the zebrafish trunk, specifically in the area between the dorsal aorta (DA) and the CV (Figure 5i and Supplementary Figure S1e). This method provided an indication of the degree of mosaicism in the mutant fish and suggested that control embryos (EV and EV + *pik3r1Mo*) had a higher integration rate than those injected with *PIK3R1*, with the exception of the *PIK3R1*^{L570P} mutant.

DISCUSSION

In this study, we describe a CM subtype, CMDV, which we found to be associated with somatic mutations in 2 genes belonging to the PI3K–Akt–mTOR signalling pathway: *PIK3R1* and *PIK3CA* (Figure 6).

In patients, the clinical phenotype primarily manifests as a common, small CM on the limbs. These CMs exhibit pale, purplish indistinct borders, which stand in contrast to the well-defined reddish borders typically observed in classic CM cases. Patients had no or limited hypertrophy of soft tissues, yet they exhibit prominent dilated cutaneous veins on the CM. Neither overgrowth nor signs of skeletal or lymphatic malformation were observed. Likely, many of these patients are now misdiagnosed as mild Klippel Trenaunay syndrome, lacking a lymphatic component. Our patient cohort, on the other hand, exhibited mild to no pain; normal levels of D-dimers; no involvement of the deep venous system; and therefore, no increased risk of thromboembolism. These characteristics serve to further differentiate them from individuals with Klippel Trenaunay syndrome. Such lesions were described earlier and recognized as capillary–venous malformations (Uihlein et al, 2013). To emphasize the predominant clinical feature, namely a CM accompanied by dilated veins, we propose to rename them CMDVs. Following the recently proposed gene–phenotype–based nomenclature (Biesecker et al, 2021), we suggest calling the CMDV lesions—when genetic data are available—PIK3R1-CMDV and PIK3CA-CMDV.

The 4 somatic variants identified in *PIK3R1* are known in cancer (Chen et al, 2018; Jaiswal et al, 2009). Typically, they are oncogenic mutations that disrupt the inhibitory activity of p85 on the p110-catalytic subunit, while maintaining the

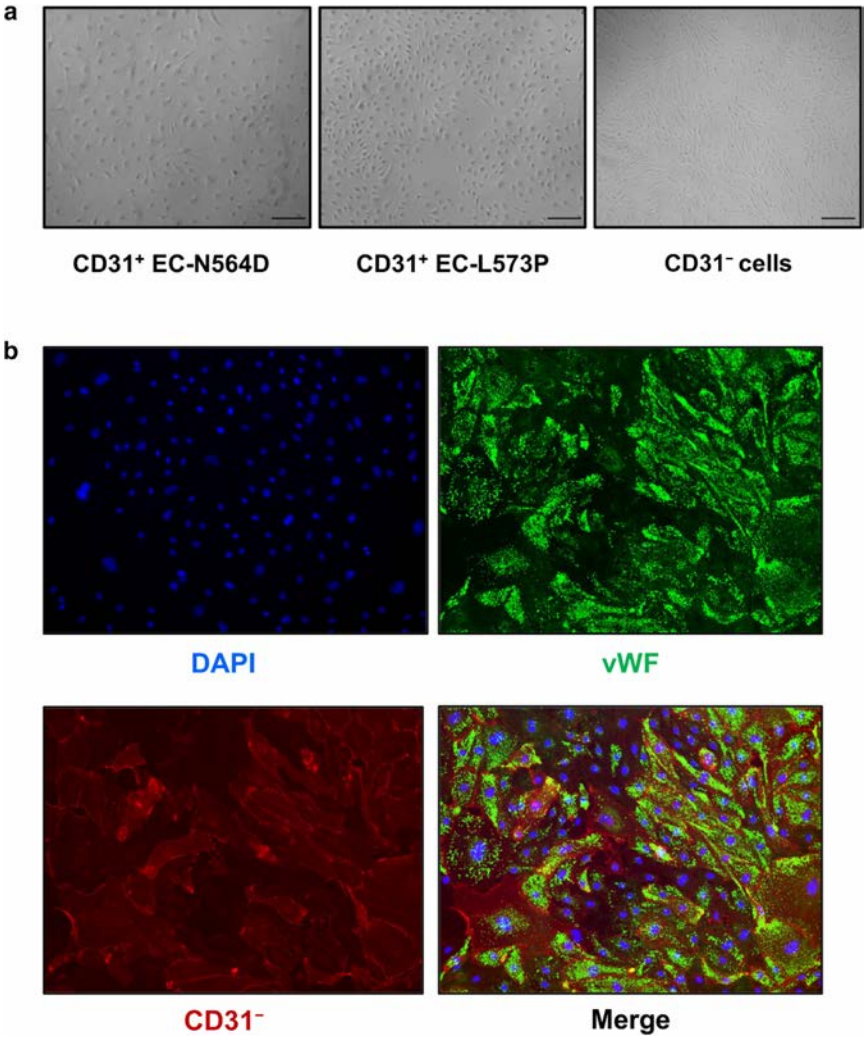

Figure 3. ECs isolated from patients with CMDV. **(a)** $CD31^+$ selected EC and $CD31^-$ cells. $CD31^+$ EC show the typical cobblestone morphology; $CD31^-$ cells look more elongated. **(b)** Immunofluorescence of $CD31^+$ selected EC expressing vWF and CD31. Bar = 1000 μM. CMDV, capillary malformation with visible dilated veins; EC, endothelial cell; vWF, von Willebrand factor.

stabilizing effect, resulting in p110-mediated activation of downstream signaling pathways (Jaiswal et al, 2009). Although the G376R and N564D variants have been characterized in vitro (Jaiswal et al, 2009; Li et al, 2021), the L570P and L573P variants are predicted to be pathogenic but lack experimental validation. *PIK3R1* variations have only recently been reported in vascular malformations, within the context of *PIK3R1*-related overgrowth syndromes that mimic *PIK3CA*-related overgrowth syndromes (Cottrell et al, 2021; Siegel et al, 2018).

The 3 variants identified in *PIK3CA* are missense somatic non-hotspot variants (allele frequency of 3−7%) localized in the C2 domain (involved in binding to the phospholipid membrane) and in the PI3K catalytic domain. Two of the 3 variants (E453K and M1043I) enhance transformation of Ba/F3 cells and induce Akt phosphorylation (Dogruluk et al, 2015; Gymnopoulos et al, 2007; Jin et al, 2021; Ng et al, 2018). This activation is weaker than that induced by the E542/545K and H1047R hotspots. Yet, this indicates that these non-hotspot variants provide driver activity. The C378Y variant remains uncharacterized.

Somatic *PIK3R1* variants were reported in a series of 12 individuals with vascular malformations. The authors had included patients with a *PIK3CA*-related overgrowth syndromes−like phenotype, consisting of capillary, venous, and lymphatic malformations; lipoma/fatty tissue overgrowth; and digital abnormalities, making it clinically difficult to distinguish them from those with *PIK3CA*-related overgrowth syndromes due to a somatic *PIK3CA* mutation (Cottrell et al, 2021). In addition, a somewhat similar cutaneous phenotype to CMDV has also been recently associated with severe focal cortical dysplasia and a variant in the *AKT3* gene (De Bortoli et al., 2024).

As the clinical and genetic spectrum of vascular anomalies continues to be defined, the clinic−genetic distinctions are becoming increasingly important. Precision therapies continue to be developed, and organotypic vessel types are acknowledged (Petrova and Koh, 2018). Thus, anomalies due to different genes and even variants in the same gene along with the different vessel types they affect in a given lesion may respond differently to therapeutic approaches.

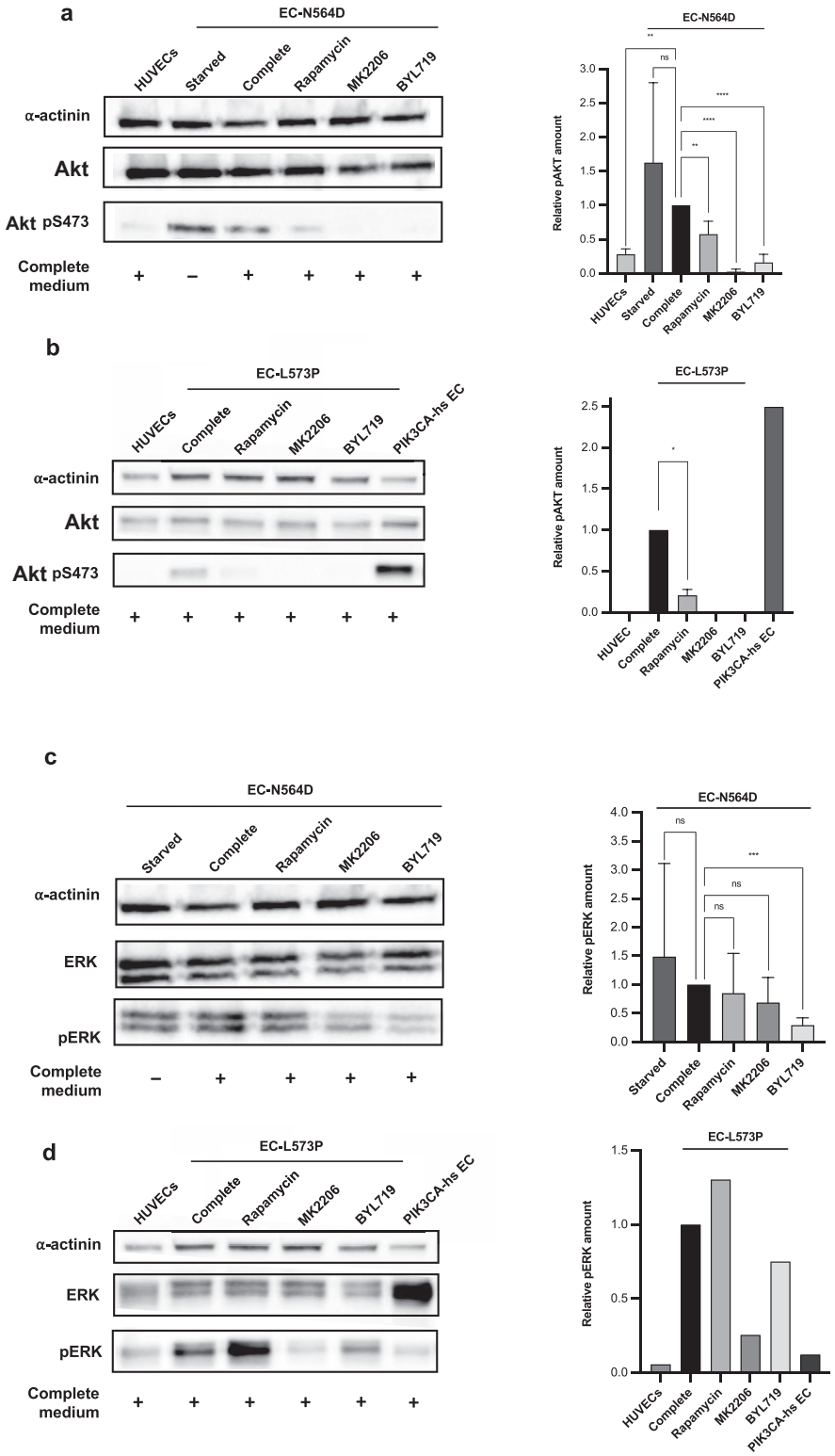

Figure 4. Western blot analysis of Akt and ERK phosphorylation and treatment with PI3K pathways inhibitors. **(a)** Patient-derived EC-N564D display Akt phosphorylation. pAkt is decreased after treatment with rapamycin and BYL719 (48 h) or MK2206 (24 h). **(b)** Patient-derived EC-L573P display Akt phosphorylation. pAkt is decreased after treatment with rapamycin and BYL719 (48 h) or MK2206 (24 h). **(c)** Patient-derived EC-N564D show ERK phosphorylation. pERK is decreased upon treatment with BYL719 but not with rapamycin or MK2206. **(d)** Patient-derived EC-L573P show ERK phosphorylation. pERK is decreased upon treatment with BYL719 and MK2206 but not with rapamycin. α-Actinin was used as loading control. PIK3CA-hs ECs are primary cells from a patient with CLVM (H1047R *PIK3CA* mutation). Error bars are shown as measure of variability and represent the SD. Experiments were repeated n = 5 times for EC-N564D cells. Owing to a shortage of surgical resected tissue and limited number of viable EC-L573P passages, Akt/pAkt and ERK/pERK were repeated n = 2 and n = 1 times, respectively. Akt, protein kinase B; CLVM, capillaro–lymphatico–venous malformation; EC, endothelial cell; ERK, extracellular signal–regulated kinase; h, hour; hs, hotspot; ns, not significant; pAkt, phosphorylated protein kinase B; pERK, phosphorylated extracellular signal–regulated kinase; PI3K, phosphoinositide 3-kinase.

Sequencing of primary ECs derived from 2 PIK3R1-CMDV patients revealed a mutant allele frequency of approximately 50%, in contrast with the lower somatic percentages detected in the corresponding tissue samples. This indicates that all the isolated ECs were likely heterozygous for the somatic mutation. This could be due to their better survival or high

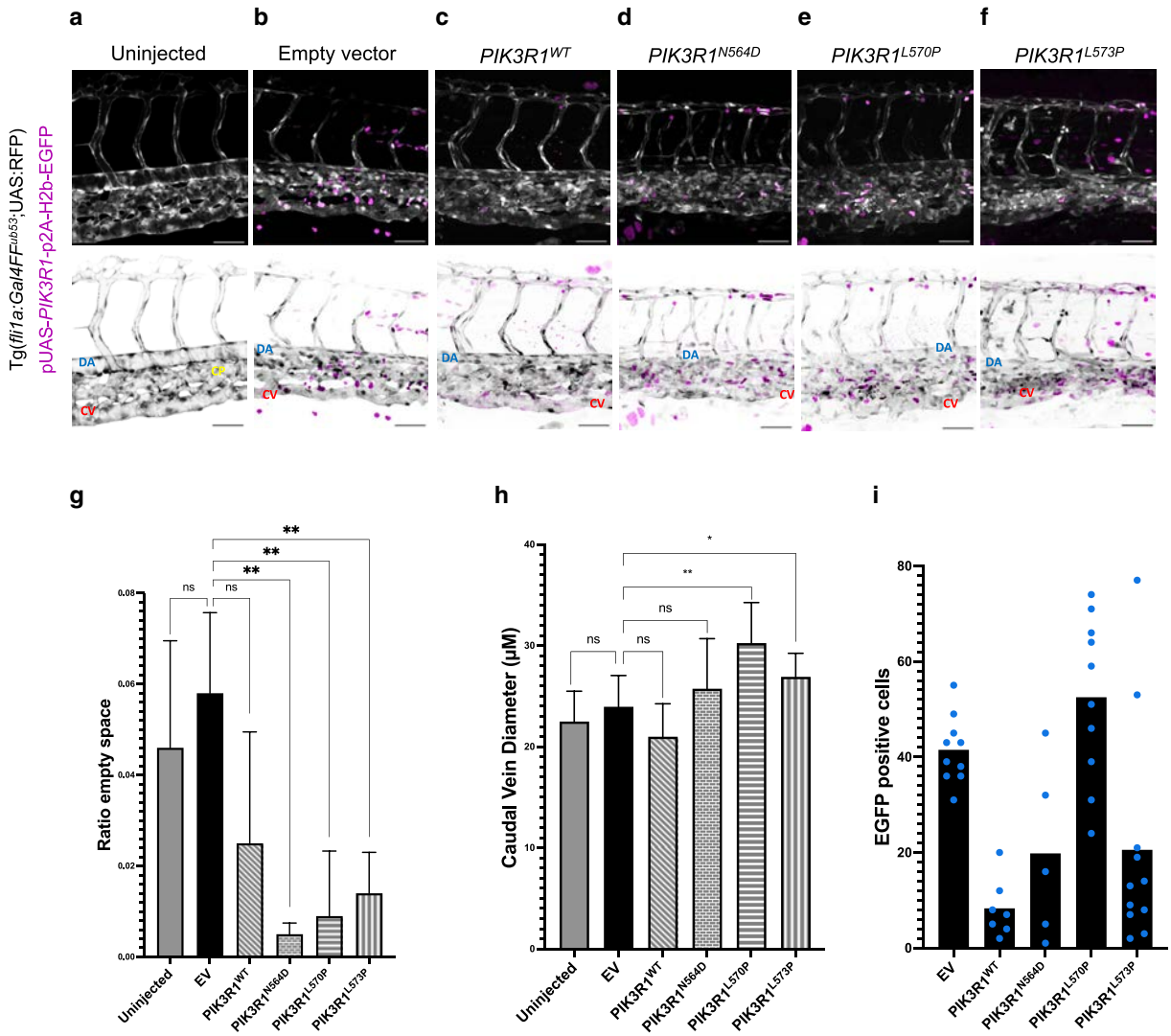

Figure 5. Endothelial-specific overexpression of mutated *PIK3R1* in *Tg(fli1a:Gal4FF^{ub53};UAS:RFP)*-positive zebrafish embryos. Normal and inverted images are shown. EGFP^{+} cells (magenta) contain the injected plasmid. CV (red), DA (yellow), and CP (blue) are shown. **(a)** Embryos with normal development of trunk vasculature. **(b, c)** Embryos injected with pUAS-p2A-H2b-EGFP (EV) and pUAS-*PIK3R1*^{WT}-p2A-H2b-EGFP: normal development of trunk vasculature. **(d–f)** Embryos injected with pUAS-*PIK3R1*-p2A-H2b-EGFP expressing mutated *PIK3R1*: CV enlargement and CP disruption. **(g)** Quantification of area between CV and DA occupied by the capillary bed: ratio between intravessel and intervessel space. **(h)** Quantification of CV diameter. **(i)** Quantification of plasmid integration rate in zebrafish endothelium: EGFP^{+} cells found in capillary–venous plexus. Plotted are averages normalized on the number of embryos for each condition. Each blue dot corresponds to 1 embryo. Bar = 50 µM. Error bars are shown as measure of variability and represent the SD. Number of biological replicates: uninjected, n = 19; EV, n = 10; *PIK3R1*^{WT}, n = 9; *PIK3R1*^{N564D}, n = 4; *PIK3R1*^{L570P}, n = 8; and *PIK3R1*^{L573P}, n = 9. Embryos in which the CV was not readily distinguishable were discarded. CV, caudal vein; CP, capillary plexus; DA, dorsal aorta; EV, empty vector; ns, not significant.

frequency of mutant ECs in the patients' resected tissue. Anyhow, the somatic mutation was not detected in the non-ECs, confirming that the source of the malformation resides within the vascular endothelium.

The *PIK3R1* c.1690A>G; N564D has previously been demonstrated to promote p110-independent cell survival, increased Akt signaling, and anchorage-independent growth of epithelial and Ba/F3 cells (Jaiswal et al, 2009; Urick et al, 2011) as well as epithelial cell proliferation in the absence of epithelial growth factor (Chen et al, 2018). To assess whether this also happens in CMDV and in primary cells, we characterized the *PIK3R1* L573P and N564D variants in patient-derived ECs. We showed an increase in pAkt and pERK, even when CMDV ECs were grown in starved conditions. This suggests that the downstream cell survival and proliferation pathways are activated as a direct consequence of the mutations, and this is not dependent on GFs. However, Akt phosphorylation was weaker in EC-N564D and EC-L573P than in *PIK3CA*-hotspot CLVM cells, underscoring the clinical distinction between the milder PIK3R1-CMDV and the more severe *PIK3CA*-hotspot manifestations.

Treatment of EC-N564D and EC-L573P with PI3K pathway inhibitors (sirolimus, MK2206, and BYL719) (Figure 4) significantly reduced pAkt levels, confirming the potential of

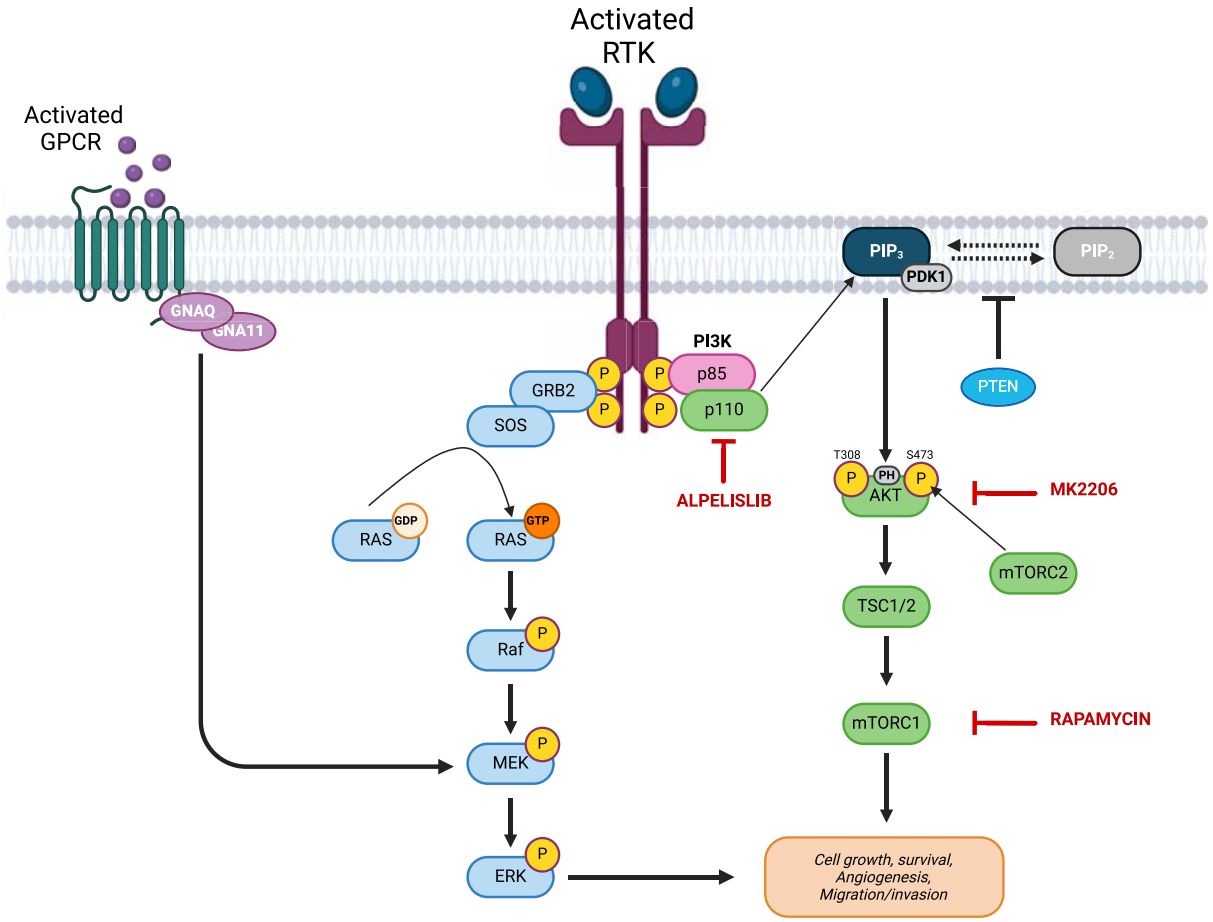

Figure 6. PI3K–Akt–mTOR signaling and RAS–RAF–MAPK signaling in vascular anomalies. Inhibitors of the signaling pathway are shown in red: PIK3CA inhibitor alpelisib (BYL719), Akt inhibitor MK-2206, and mTOR inhibitor rapamycin (sirolimus). Akt, protein kinase B; ERK, extracellular signal–regulated kinase; MEK, MAPK/extracellular signal–regulated kinase; PI3K, phosphoinositide 3-kinase.

pre-existing cancer drug for treating CMDV. In EC-N564D, pERK levels were not decreased by the mTOR and Akt inhibitors because these targets are not part of the MAPK pathway. However, we found BYL719 to be very effective in reducing pERK levels. This suggests that cross-talk between PI3K and MAPK pathways could take place at the level of PI3K, right after the binding of the ligand to the RTK and the activation of the cytosolic kinases. Altogether, these data suggest that *PIK3R1* mutations in ECs are sufficient to trigger the activation of the PI3K and MAPK pathways, and the inhibition of the upstream PI3K kinase is enough to block both cascades.

Zebrafish has already been used to model vascular malformations (Al-Olabi et al, 2018; Bell et al, 2021). We thus next employed it to replicate CMDV manifestations in vivo. Endothelium-specific mosaic embryos that exclusively expressed the transgene in the vasculature allowed us to mimic the conditions of patients with mosaic CMDV. Two main phenotypes, recapitulating the manifestations of patients with CMDV, were observed in mutant embryos: (i) enlargement of the CV diameter and (ii) disruption of the capillary network.

Specifically, enlarged CV occurred only in cases of complete *PIK3R1* knockdown as well as upon overexpression of 2 of 3 mutant *PIK3R1*, suggesting these variants to be loss of function. We attribute the lack of statistical significance for the *PIK3R1*^{N564D} variant to the substantial variability in the mosaicism levels among embryos. Assessment of cell size, based on measurements of the average distance between EGFP^{+} nuclei, showed no increase in cell size in mutants compared with that in control embryos (Supplementary Figure S3). This suggests proliferation rather than a change in cell size as the mechanism underlying the enlarged CV diameter. Embryos lacking a clearly distinguishable CV were omitted from the analysis. Notably, the proportion of excluded embryos was higher in mutant embryos than in control or WT ones (Supplementary Table S1). This underscores pathophysiological effect also for N564D variant in which the percentage of discarded embryos reached 42.8%, compared with 0% for empty vector and 10% and 6.25% for the WT and WT + *pik3r1Mo* constructs, respectively. Despite the clonal expression, we only noted a tendency toward a compressed capillary bed in embryos with knocked down expression, in contrast to the consistently pronounced

phenotype observed in embryos overexpressing mutant *PIK3R1*. Although this tendency in knocked down embryos did not reach statistical significance, it still led to observable alterations in the overall appearance of the caudal region. Overall, this indicates that the phenotype can be induced by mutant *PIK3R1* alone and that malformations are not due to a dosage effect. Indeed, overexpressing *PIK3R1*^{WT} did not result in malformations. Therefore, we hypothesize that the mosaic mutations act through a dominant mechanism on the pool of endogenous *PIK3R1*^{WT} by adversely affecting its regulatory activity on the p110 subunit. In short, mosaic overexpression of mutated *PIK3R1* is sufficient to induce a phenotype in embryos, despite the presence of endogenous *PIK3R1*. Furthermore, in the rescue experiment, we did not observe an improvement nor an exacerbation of the phenotype induced by the morpholino when attempting to rescue it with WT or mutated *PIK3R1*. This can be attributed to the fact that whereas the morpholino targeted the entire pool of endogenous *PIK3R1*, the plasmid induced only mosaic expression, which varied from embryo to embryo, and it was not integrated in all cells. Therefore, the relatively low mosaicism level of the injected constructs did not allow for a modulation of the generalized effect of the morpholino. However, we observed that mutant embryos with higher rate of plasmid integration and thus with a higher number of EGFP^{+} cells showed a tendency toward a more severe malformation (data not shown). These observations further support the hypothesis that *PIK3R1* pathogenic variants result in a dominant *PIK3R1* function.

We observed a strong specificity of the malformations for slow-flow vessels in zebrafish. Despite the presence of mutated *PIK3R1*-expressing cells (EGFP^{+}) across different structures, including CV and capillary plexus, DA, intersegmental vessels, and dorsal longitudinal anastomotic vessels, the abnormal phenotype was limited to the CV and capillary plexus. This suggests that fast-flow vessels, such as the DA, might be protected against the development of vascular abnormalities induced by *PIK3R1* mutations. This aligns with clinical observations, where CMDV malformations predominantly impact veins and capillaries, whereas arteries remain unaffected. However, further investigation is needed to gain a deeper understanding of this potential mechanism. In summary, we identified that CM associated with dilated veins (CMDV) is due to somatic *PIK3R1* or non-hotspot *PIK3CA* pathogenic variants. Our findings suggest that somatic dominant *PIK3R1* and non-hotspot *PIK3CA* mutations could serve as a global mechanism for activation of class IA PI3Ks, leading to CMDV. On the basis of primary cell isolations, we propose that the phenotype originates from mutant ECs, which are an accessible target through the circulation. Currently, the management of CM typically involves laser ablation and surgery. However, our discovery on the mutated genes and dysregulated pathways underlying CMDV opens avenues for potential treatment of this condition using anticancer drugs targeting PI3K signalling. In addition, in vivo studies recapitulating the capillary–venous–specific phenotype observed in patients indicate zebrafish as a potential model for future drug screenings.

MATERIALS AND METHODS

Patient population and study approval

Written informed consent was obtained from all participants and approved by the ethical committee of the Medical Faculty at the University of Louvain (Brussels, Belgium) (B403201629786) and the Centre Hospitalier Universitaire de Caen (Caen, France). All subjects or their parent/guardian included in this study consented to publication of the images in Figure 2.

Sample collection and DNA extraction

Our cohort consisted of 82 CM tissue samples. Tissue biopsies were collected during programmed surgeries and snap frozen in liquid nitrogen or placed in RNAlater solution (Thermo Fisher Scientific). DNA from biopsies was extracted using the Wizard Genomic DNA-purification kit (Promega), as previously described (Limaye et al, 2015).

Next-generation sequencing of tissular DNA and primary EC and variant analysis

DNA samples were screened using IonTorrent technology, with 2 IonAmpliseq in-house designed panels (Thermo Fisher Scientific) containing genes belonging to pathways involved in vascular anomalies. Libraries were prepared using the Ion AmpliSeq Library Kit 2.0, according to manufacturer's instructions (publication number MAN006735, Life Technologies). Theoretical vertical coverage was set to a minimum of 1000×. Raw data were aligned against the human reference genome (hg19/GRCh37) using Ion Torrent Suite Server 5 (Life Technologies). Variants were called using the Torrent variant caller (version 5.8.0). Stringent filtering of the variants was performed with in-house developed software, Highlander (https://sites.uclouvain.be/highlander/). DNA was extracted from CD31^{+} EC and CD31^{-} cells using Wizard Genomic DNA Purification Kit (Promega). Cells were sequenced through targeted next-generation sequencing (1000×) and whole-exome sequencing (median vertical coverage of 229×). Sanger sequencing was performed to confirm next-generation sequencing results.

Cell culture, isolation of primary EC, and treatment with signaling pathway inhibitors

Primary ECs from patients with CMDV and CLVM were isolated from patient tissues. Dissociated cells were grown on fibronectin-coated plates in Endothelial Cell Growth Medium 2 (Bio-Connect) containing penicillin/streptomycin (Sigma-Aldrich). ECs were isolated using antibodies against CD31 coupled to magnetic beads (Miltenyi). ECs and HUVECs were cultured on fibronectin-coated (Millipore) plates in Endothelial Cell Growth Medium 2. CD31-negative cells were also kept and separately cultured in the same conditions. Cells were treated with 15 nM rapamycin (LC Laboratories), 5 μM BYL719 (LC Laboratories) for 48 hours, or 1 μM MK2206 (Bio-Connect) for 24 hours. For starvation experiments, cells were grown in Endothelial Cell Basal Medium 2 without fetal cals serum and GFs for 48 hours.

Immunofluorescence

Cells were grown on fibronectin-coated chamber slides (Sigma-Aldrich), fixed with acetone, and stained with antibodies against CD31 and von Willebrand factor (1:500, Dako). Rabbit Alexa488 or mouse Alexa594 were used as secondary antibodies (1:500, Thermo Fisher Scientific). Injected zebrafish embryos were selected to keep only those displaying fluorescent signal in vasculature and fixed in 4% paraformaldehyde and stained for chicken anti-GFP (1:200, Aves

Labs) and subsequently, for FITC-conjugated goat anti-chicken (1:200, Aves Labs). Images were captured on a fluorescent microscope (Leica) or on LSM710 (Zeiss) and processed with Fiji (version 2.9.0).

Western blot analyses

Cell lysates from nontreated or drug-treated CMDV ECs, CLVM ECs, and HUVECs were analyzed by western blot. Quantification was performed using ImageJ. Statistical analyses were performed using GraphPad Prism 9.5.9. An unpaired 2-tailed *t*-test with Welch's correction was used.

Site-specific mutagenesis of *PIK3R1*

Human *PIK3R1* (NM_181523.2) cDNA was synthesized from total RNA extracted from human tissue, cloned into pBlueScript II SK(+) vector. Mutagenesis was performed through PCR. The whole coding sequence was sequenced to verify the absence of undesired changes. *PIK3R1*^{WT} and mutant cDNAs were then transferred into the linearized UAS-p2A-H2B-EGFP expression vector.

Zebrafish strains

Handling of zebrafish was done according to FELASA guidelines (Aleström et al, 2020) (Laboratory animals 54 [3], 213-224) in compliance with German and Brandenburg state laws, monitored by local authority for animal protection (Landesamt für Arbeitsschutz, Verbraucherschutz und Gesundheit, Brandenburg, Germany).

Plasmid and morpholino injection into zebrafish embryos

A total of 1 nl of injection mixture (plasmid and Tol2-transposase mRNA) was injected into embryos at 1-cell stage. Empty vector UAS-H2B-EGFP was injected in the same manner, as negative control. A total of 5 ng of splicing-inhibiting morpholino *pik3r1Mo* or *std-Mo* were injected for knockdown experiments. Knockdown efficiency was confirmed by RT-PCR from cDNA of injected embryos. For rescue experiments of endogenous *PIK3R1* knockdown, injection mixture containing the expression vector and *pik3r1Mo/std-Mo* in the same concentrations were injected into 1-cell stage embryos. Confocal images were obtained using LSM 710 or LSM 880 Airyscan confocal laser microscopes (Zeiss) and ZEN 2 software (×40 objective).

Quantification of CV diameter, vascular bed breadth, and extravascular space

The diameter of the embryonic zebrafish CV was measured using Fiji. Three measurements were taken on each embryo (left, center, and right side of the image). Comparisons were made using unpaired 2-tailed *t*-test with Welch's correction (GraphPad Prism 9.5.9). Detection of the extravascular space was performed on maximum intensity Z-projection images using an in-house developed script on the basis of EBImage (Pau et al, 2010), Reshape (Wickham, 2007), and Raster (Hijmans and van Etten, 2012) scripts, which allowed to circle and assign an identification to each empty space between vessels. This analysis was performed on n = 5 embryos per condition and was only focused on the area in between DA (excluded) and CV (included).

Plasmid integration rate analysis

The rate of plasmid integration was determined by counting nuclei with EGFP (EGFP^{+}) expression. We counted nuclei between DA (excluded) and CV (included). The counting was performed on confocal Z-stack images of the EGFP channel. SDs are reported as measure of variability.

DATA AVAILABILITY STATEMENT

Data are available upon reasonable request. All data relevant to the study are included in the article or uploaded as supplementary information. The datasets supporting this study have not been deposited in a public repository because data are not public owing to privacy laws on patients. Some of the data may be requested by contacting to corresponding author.

ORCIDs

Martina De Bortoli: http://orcid.org/0009-0002-2455-1731
Angela Queisser: http://orcid.org/0000-0002-0993-9132
Van Cuong Pham: http://orcid.org/0000-0003-4787-7013
Anne Dompmartin: http://orcid.org/0000-0003-0081-500X
Raphaël Helaers: http://orcid.org/0000-0002-7046-7867
Simon Boutry: http://orcid.org/0000-0002-3214-2981
Cathy Claus: http://orcid.org/0009-0005-7560-7020
Frank Hammer: http://orcid.org/0000-0003-0745-3830
An-Katrien De Roo: http://orcid.org/0000-0002-0000-1260
Pascal Brouillard: http://orcid.org/0000-0001-9548-8229
Salim Abdelilah-Seyfried: http://orcid.org/0000-0003-3183-3841
Laurence M. Boon: http://orcid.org/0000-0001-8273-3328
Miikka Vikkula: http://orcid.org/0000-0002-6236-338X

CONFLICT OF INTEREST

The authors state no conflict of interest.

ACKNOWLEDGMENTS

Four of the authors of this publication are members of the VASCA Working Group of the European Reference Network for Rare Multisystemic Vascular Diseases (project identification 769036). We are grateful to all the family members for their invaluable participation. The authors thank Audrey Debue and Fabrice Cahay for expert technical assistance. These studies were financially supported by the Fonds de la Recherche Scientifique (grants T.0240.23 and P.C005.22 to MV and T.0146.16 and P.C013.20 to LMB) and by the Fund Generet managed by the King Baudouin Foundation (grant 2018-J1810250-211305), the Walloon Region through the FRFS-WELBIO strategic research programme (WELBIO-CR-2019C-06), and the European Union's Horizon 2020 research and innovation programme under grant agreement number 874708 (Theralymph) (all to MV). This project was also funded by the Swiss National Science Foundation under the Sinergia project nro CRSII5_193694 (LMB/MV). The project has also received funding from the European Union's Horizon 2020 research and innovation programme under the Marie Skłodowska-Curie grant agreement number 814316 (project VACure) and Leducq Foundation Networks of Excellence Program grant ReVAMP (LFCR Grant 21CVD03) (both to SA-S and MV). PB is a scientific logistics manager of the Genomics Platform of University of Louvain. The project was also supported by a Pierre M. fellowship. The authors thank the Genomics Platform of University of Louvain for IonTorrent PGM next-generation sequencing. We also thank the National Lottery of Belgium and the Foundation against Cancer (2010-101) for their support to the Genomics Platform of University of Louvain and de Duve Institute as well as the Fonds de la Recherche Scientifique (FNRS equipment grant U.N035.17) for the Big data analysis cluster for next-generation sequencing at University of Louvain.

AUTHOR CONTRIBUTIONS

Conceptualization: MDB, PB, AQ, SA-S, MV; Data Curation: MDB, VCP, SB, RH, PB, AQ, MV; Formal Analysis: MDB, AQ, VCP; Resources: MV; Software: RH; Supervision: SA-S, MV; Writing - Original Draft Preparation: MDB; Writing - Review and Editing: MDB, PB, SA-S, A-KDR, MV

SUPPLEMENTARY MATERIAL

Supplementary material is linked to the online version of the paper at www.jidonline.org, and at https://doi.org/10.1016/j.jid.2024.01.033.

REFERENCES

Adams DM, Trenor CC, Hammill AM, Vinks AA, Patel MN, Chaudry G, et al. Efficacy and safety of sirolimus in the treatment of complicated vascular anomalies. Pediatrics 2016;137:e20153257.

Aleström P, D'Angelo L, Midtlyng PJ, Schorderet DF, Schulte-Merker S, Sohm F, et al. Zebrafish: housing and husbandry recommendations. Lab Anim 2020;54:213–24.

Al-Olabi L, Polubothu S, Dowsett K, Andrews KA, Stadnik P, Joseph AP, et al. Mosaic RAS/MAPK variants cause sporadic vascular malformations which respond to targeted therapy [published correction appears in J Clin Invest 2018;128:5185] J Clin Invest 2018;128:1496–508.

Amyere M, Revencu N, Helaers R, Pairet E, Baselga E, Cordisco M, et al. Germline loss-of-function mutations in EPHB4 cause a second form of capillary malformation-arteriovenous malformation (CM-AVM2) deregulating RAS-MAPK signaling. Circulation 2017;136:1037–48.

Bell LM, Holm A, Matysiak U, Driever W, Rößler J, Schanze D, et al. Functional assessment of two variants of unknown significance in TEK by endothelium-specific expression in zebrafish embryos. Hum Mol Genet 2021;31:10–7.

Biesecker LG, Adam MP, Alkuraya FS, Amemiya AR, Bamshad MJ, Beck AE, et al. A dyadic approach to the delineation of diagnostic entities in clinical genomics. Am J Hum Genet 2021;108:8–15.

Boon LM, Dekeuleneer V, Coulie J, Marot L, Bataille A-C, Hammer F, et al. Case report study of thalidomide therapy in 18 patients with severe arteriovenous malformations. Nat Cardiovasc Res 2022;1:562–7.

Boscolo E, Limaye N, Huang L, Kang KT, Soblet J, Uebelhoer M, et al. Rapamycin improves TIE2-mutated venous malformation in murine model and human subjects. J Clin Invest 2015;125:3491–504.

Brouillard P, Schlögel MJ, Homayun Sepehr N, Helaers R, Queisser A, Fastré E, et al. Non-hotspot PIK3CA mutations are more frequent in CLOVES than in common or combined lymphatic malformations. Orphanet J Rare Dis 2021;16:267.

Chen L, Yang L, Yao L, Kuang XY, Zuo WJ, Li S, et al. Characterization of PIK3CA and PIK3R1 somatic mutations in Chinese breast cancer patients. Nat Commun 2018;9:1357.

Cottrell CE, Bender NR, Zimmermann MT, Heusel JW, Corliss M, Evenson MJ, et al. Somatic PIK3R1 variation as a cause of vascular malformations and overgrowth. Genet Med 2021;23:1882–8.

Couto JA, Huang L, Vivero MP, Kamitaki N, Maclellan RA, Mulliken JB, et al. Endothelial cells from capillary malformations are enriched for somatic GNAQ mutations. Plast Reconstr Surg 2016;137:77e–82e.

De Bortoli M, Ivars M, Revencu N, et al. Epilepsy with faint capillary malformation or reticulated telangiectasia associated with mosaic AKT3 pathogenic variants. Am J Med Genet A 2024:e63551. https://doi.org/10.1002/ajmg.a.63551.

Dogruluk T, Tsang YH, Espitia M, Chen F, Chen T, Chong Z, et al. Identification of variant-specific functions of PIK3CA by rapid phenotyping of rare mutations. Cancer Res 2015;75:5341–54.

Eerola I, Boon LM, Mulliken JB, Burrows PE, Dompmartin A, Watanabe S, et al. Capillary malformation–arteriovenous malformation, a new clinical and genetic disorder caused by RASA1 mutations. Am J Hum Genet 2003;73:1240–9.

Goss JA, Konczyk DJ, Smits P, Sudduth CL, Bischoff J, Liang MG, et al. Diffuse capillary malformation with overgrowth contains somatic PIK3CA variants. Clin Genet 2020;97:736–40.

Gymnopoulos M, Elsliger MA, Vogt PK. Rare cancer-specific mutations in PIK3CA show gain of function. Proc Natl Acad Sci USA 2007;104:5569–74.

Harbers VEM, Zwerink LGJM, Rongen GA, Klein WM, van der Vleuten CJM, van Rijnsoever IMP, et al. Clinical differences in sirolimus treatment with low target levels between children and adults with vascular malformations – A nationwide trial. Clin Transl Sci 2023;16:781–96.

Hijmans RJ, van Etten J. raster: Geographic analysis and modeling with raster data. R package version 2.0-12. 2012. http://CRAN.R-project.org/package=raster. (accessed March 18, 2024).

Jaiswal BS, Janakiraman V, Kljavin NM, Chaudhuri S, Stern HM, Wang W, et al. Somatic mutations in p85α promote tumorigenesis through class IA PI3K activation. Cancer Cell 2009;16:463–74.

Jin N, Keam B, Cho J, Lee MJ, Kim HR, Torosyan H, et al. Therapeutic implications of activating noncanonical PIK3CA mutations in head and neck squamous cell carcinoma. J Clin Invest 2021;131:e150335.

Jordan M, Carmignac V, Sorlin A, Kuentz P, Albuisson J, Borradori L, et al. Reverse phenotyping in patients with skin capillary malformations and mosaic GNAQ or GNA11 mutations defines a clinical spectrum with genotype-phenotype correlation. J Invest Dermatol 2020;140:1106–10.e2.

Keppler-Noreuil KM, Parker VE, Darling TN, Martinez-Agosto JA. Somatic overgrowth disorders of the PI3K/AKT/mTOR pathway & therapeutic strategies. Am J Med Genet C Semin Med Genet 2016;172:402–21.

Li X, Lau AYT, Ng ASN, Aldehaiman A, Zhou Y, Ng PKS, et al. Cancer-associated mutations in the p85α N-terminal SH2 domain activate a spectrum of receptor tyrosine kinases. Proc Natl Acad Sci USA 2021;118:e2101751118.

Limaye N, Kangas J, Mendola A, Godfraind C, Schlögel MJ, Helaers R, et al. Somatic activating PIK3CA mutations cause venous malformation. Am J Hum Genet 2015;97:914–21.

Nakashima M, Miyajima M, Sugano H, Iimura Y, Kato M, Tsurusaki Y, et al. The somatic GNAQ mutation c.548G>A (p.R183Q) is consistently found in Sturge-Weber syndrome. J Hum Genet 2014;59:691–3.

Ng PK, Li J, Jeong KJ, Shao S, Chen H, Tsang YH, et al. Systematic functional annotation of somatic mutations in cancer. Cancer Cell 2018;33:450–62.e10.

Pau G, Fuchs F, Sklyar O, Boutros M, Huber W. EBImage—an R package for image processing with applications to cellular phenotypes. Bioinformatics 2010;26:979–81.

Petrova TV, Koh GY. Organ-specific lymphatic vasculature: from development to pathophysiology. J Exp Med 2018;215:35–49.

Queisser A, Seront E, Boon LM, Vikkula M. Genetic basis and therapies for vascular anomalies. Circ Res 2021;129:155–73.

Seront E, Biard JM, Van Damme A, Revencu N, Lengelé B, Schmitz S, et al. A case report of sirolimus use in early fetal management of lymphatic malformation. Nat Cardiovasc Res 2023;2:595–9.

Siegel DH, Cottrell CE, Streicher JL, Schilter KF, Basel DG, Baselga E, et al. Analyzing the genetic spectrum of vascular anomalies with overgrowth via cancer genomics. J Invest Dermatol 2018;138:957–67.

Uebelhoer M, Boon LM, Vikkula M. Vascular anomalies: from genetics toward models for therapeutic trials. Cold Spring Harb Perspect Med 2012;2:a009688.

Uihlein LC, Liang MG, Fishman SJ, Alomari AI, Mulliken JB. Capillary-venous malformation in the lower limb. Pediatr Dermatol 2013;30:541–8.

Urick ME, Rudd ML, Godwin AK, Sgroi D, Merino M, Bell DW. PIK3R1 (p85α) is somatically mutated at high frequency in primary endometrial cancer. Cancer Res 2011;71:4061–7.

Walton RG, Jacobs AH, Cox AJ. Pigmented lesions in newborn infants. Br J Dermatol 1976;95:389–96.

Wickham H. Reshaping Data with the reshape Package. J Stat Softw 2007:21.

SUPPLEMENTARY MATERIALS AND METHODS

Sample collection and DNA extraction

Samples of patients with a capillary malformation were collected at Saint Luc University Hospitals in Brussels (Belgium) and at the Centre Hospitalier Universitaire de Caen (France). Our cohort consisted of a total of 82 capillary malformation tissue samples. Tissue biopsies were collected during programmed surgeries and snap frozen in liquid nitrogen or placed in RNAlater solution (Thermo Fisher Scientific). DNA from biopsies was extracted using the Wizard Genomic DNA purification-kit (Promega), as previously described (Limaye et al, 2015). DNA was subsequently quantified using NanoDrop 8000 (Thermo Fisher Scientific) and Qubit 2.0 (Thermo Fisher Scientific).

Targeted next-generation sequencing of tissular DNA and variant analysis

DNA samples were screened using IonTorrent technology with 2 IonAmpliseq in-house designed panels (Thermo Fisher Scientific). Both panels contained genes belonging to pathways involved in vascular anomalies, such as phosphoinositide 3-kinase (PI3K) and MAPK signaling. Libraries were prepared using the Ion AmpliSeq Library Kit 2.0, according to the manufacturer's instructions (publication number MAN006735, Life Technologies). For high-quality DNA extracted from fresh frozen tissues, 25 ng of DNA were employed for each of the 2 primer pools (2×). The kit-generated libraries composed of amplicons of around 180–200 pb. For low-quality DNA extracted from RNAlater samples, 10 ng of DNA for each of the 2 primer pools (5×) were employed. The kit-generated libraries composed of amplicons of around 100–110 pb.

DNA sequencing was performed on an Ion Proton sequencer (Thermo Fisher Scientific). Theoretical vertical coverage was set to a minimum of 1000×. Raw data were aligned against the human reference genome (hg19/GRCh37) using the Ion Torrent Suite Server 5 (Life Technologies) to generate .bam (binary alignment map) files. Variants were called using the Torrent variant caller (version 5.8.0). Filtering of the variants was performed with our in-house developed software, Highlander (https://sites.uclouvain.be/highlander/). Applied filters allowed to obtain variants fulfilling all the following criteria: (i) passed quality control; (ii) missense, non-sense, and consensus splice site changes; (iii) <0.005% allele frequency in the gnomAD database, including whole-exome sequencing data from 125,748 unrelated individuals (https://gnomad.broadinstitute.org/; (iv) not detected in >100 samples from individuals with unrelated pathologies in the in-house database of 1737 somatic samples; (v) >1% of alternative allele on the total coverage; (vi) >5 alternative reads on the total of depth reads; and (vii) for missense variants, predicted to affect protein function by at least 5 of 20 algorithms available in Highlander (Mutation Taster, FATHMM, FATHMM-XF, Polyphen2, Provean, SIFT4G, Mutation Assessor, MCAP, LRT, Lists2, Deogen, ClinPred, BayesDel, PrimateAI, MetaSVM, CADD phred, VEST, REVEL, MVP, MutPred). Variants present in the COSMIC (Catalogue Of Somatic Mutations In Cancer) (https://cancer.sanger.ac.uk/cosmic) database were considered as particularly relevant.

Cell culture, isolation of primary endothelial cells, and treatment with signaling pathway inhibitors

Primary endothelial cells (ECs) from patients with capillary malformation with dilated veins and capillaro–lymphatico–venous malformation were isolated from tissues by cutting them into small pieces (1–3 cm^2) and digesting with a mixture of 0.04% dispase II (Gibco), 0.25% collagenase A (Sigma-Aldrich), and 0.01% DNAse I (Sigma-Aldrich). Dissociated cells were grown on fibronectin-coated (Millipore) plates in Endothelial Cell Growth Medium 2 containing penicillin/streptomycin (Sigma-Aldrich) until confluency. ECs were isolated using an antibody against CD31 coupled to magnetic beads (Miltenyi), and the obtained $CD31^+$ cells were cultured on fibronectin-coated plates in Endothelial Cell Growth Medium 2. $CD31^-$ cells were also kept and separately cultured in the same conditions. Cobblestone cell morphology of the $CD31^+$ cells was determined using a bright field microscope (Zeiss). For drug testing, ECs were grown in complete medium and treated with 15 nM rapamycin (LC Laboratories) or 5 μM BYL719 (LC Laboratories) for 48 hours or with 1 μM MK2206 (Bio-Connect) for 24 hours. For starvation experiments, ECs were grown in Endothelial Cell Basal Medium-2 without fetal calf serum and GFs for 48 hours. Human umbilical vein endothelial cells were grown on fibronectin-coated plates in complete Endothelial Cell Growth Medium 2 (Bio-Connect). Experiments were only performed twice for EC-L573P owing to shortage of surgical resected tissue and limited number of passages after which ECs continue to grow.

Cell immunofluorescence

Cells were grown on fibronectin-coated chamber slides (Sigma-Aldrich), fixed with acetone, and stained with antibodies against CD31 and von Willebrand factor (1:500, Dako). Rabbit Alexa 488 or mouse Alexa 594 were used as secondary antibodies, respectively (1:500, Thermo Fisher Scientific). Images were captured on a fluorescent microscope (Leica).

Sequencing of DNA extracted from primary cells

DNA was extracted from $CD31^+$ ECs as well as from $CD31^-$ cells using the Wizard Genomic DNA Purification Kit (Promega). Besides Targeted next-generation sequencing, DNA underwent whole-exome sequencing using the Twist capture-kit and Illumina sequencing on a Novaseq machine (performed by Macrogen), achieving a median vertical coverage of 229×. Sequences were aligned to the reference human genome (hg38) and processed with Highlander, as described earlier. Sanger sequencing was performed to confirm the *PIK3R1* next-generation sequencing results through Eurofins Genomics, with the following primers: forward 5′-GACAGGAAGAGAAGCCACGC-3′ and reverse 5′-GCCCAACCACTCGTTCAACTTC-3′. Chromatograms were analyzed using CLC Main Workbench (Qiagen).

Western blot analyses

Cell lysates from nontreated or drug-treated capillary malformation with dilated veins ECs, capillaro—lymphatico—venous malformation ECs, human umbilical vein endothelial cells, and HUVEC$^{PIK3CA\text{-}E545K}$ were analyzed by western blot using antibodies against α-actinin (1:1000, number 6487, Cell Signaling Technologies), protein kinase B (1:1000, number 9272, Cell Signaling Technologies), phosphorylated protein kinase B Ser473 (1:1000, number 9271, Cell Signaling Technologies), p44/42 MAPK (extracellular signal—regulated kinase1/2) (1:1000, number 9102, Cell Signaling Technologies), and phosphorylated p44/42 MAPK (extracellular signal—regulated kinase 1/2) Thr202/Tyr204 (number 9101, Cell Signaling Technologies). Quantification was performed using ImageJ. Statistical analysis of western blot quantification data was performed using GraphPad Prism (version 9.5.9). An unpaired 2-tailed *t*-test with Welch's correction was used.

Zebrafish strains

Handling of zebrafish was done according to Federation of European Laboratory Animal Science Associations guidelines (Westerfield et al, 1997), in compliance with German and Brandenburg state laws, carefully monitored by the local authority for animal protection (Landesamt für Arbeitsschutz, Verbraucherschutz und Gesundheit, Brandenburg, Germany). The following stable lines of zebrafish were maintained under standard conditions as previously described (Westerfield et al, 2000): *Tg(kdrl:EGFP)*^{s843} (Jin et al, 2005), *Tg(fli1a:Gal4FF)*^{ubs3} (Herwig et al, 2011), *Tg(UAS:RFP)*^{nkuasrfp1a} (Asakawa et al, 2008), and *Tg(UAS:lifeactRFP)*^{mu262} (Rödel et al, 2019).

Site-specific mutagenesis of *PIK3R1*

Human *PIK3R1* (NM_181523.2) cDNA was synthesized from total RNA extracted from human tissue using RevertAid H Minus First Strand cDNA Synthesis kit (Thermo Fisher Scientific, number K1632) cloned into the pBlueScript II SK vector by EcoRI restriction enzyme cloning. Mutagenesis primers were designed using the QuikChange II XL Primer Design-tool (Agilent). In vitro site-directed mutagenesis was performed through PCR using Pfu Turbo polymerase (Thermo Fisher Scientific, number EP0501) followed by *DpnI* enzyme digestion. The whole coding sequence of the gene was sequenced to confirm the presence of the nucleotide change of interest and exclude undesired changes. *PIK3R1* wild type and mutant cDNAs were transferred into the linearized UAS-p2A-H2B-EGFP expression vector using the In-Fusion Snap Assembly Master Mix (Takara Bio, number 638954), following manufacturer's instructions (primers: 5′-CACACGAATTCCTGCAGCCCATGAGTGCTGAGGGGTACCAGTA-3′ forward and 5′-AAATTAGTAGCACCAGAACC-TCGCCTCTGCTGTGCATATACTG-3′ reverse). Plasmids were purified with the PureYield Plasmid Midiprep System (Promega, number A2492) and sequence verified.

Plasmid and morpholino injection into zebrafish embryos

Plasmids were prepared in an injection mixture containing 20 ng/μl of plasmid and 20 ng/μl of Tol2-transposase mRNA (coinjected to facilitate genomic integration of the plasmid). The plasmid was based on a UAS promoter, followed by the gene of interest. A total of 1 nl of injection mixture (plasmid and Tol2-transposase mRNA) was injected into transgenic Tg(fli1a:Gal4FF)$^{ubs3/+}$ embryos at 1-cell stage to overexpress *PIK3R1* variants specifically in endothelial cells with the GAL4-UAS system. In addition, we used the combination of transgenic lines Tg(fli1a:Gal4FF)$^{ubs3/+}$;Tg(UAS:RFP)$^{nkuasrfp1a/+}$ to confirm the Gal4 presence on the basis of the expression of RFP fluorescent proteins. Empty vector of UAS-H2B-EGFP was injected in the same manner, as a negative control. For endogenous *Pik3r1* knockdown experiments, either 5 ng of splicing inhibiting morpholino *Pik3r1MO* (5′-GTATGGTATATTTACCTGGAGCTGC-3′; GeneTools, LLC) (1 ng of 0.59 mM, refer to Nicoli et al [2012], or equivalent amount of standard control morpholino std-MO (5′-CCTCTTACCTCAGTTACAATTTATA-3′; GeneTools, LLC) was injected into 1-cell staged embryos. Knockdown efficiency was confirmed by semiquantitative RT-PCR from cDNA of injected embryos using the following primers: forward 5′-CCCAGCACTCTTCAGACATC-3′ and reverse 5′-TTTAGTGGAGGCATCTCGGA-3′). Assessment of the disappearance of endogenous amplified fragment was performed on agarose gel. For rescue experiments of endogenous *Pik3r1* knockdown, injection mixes containing plasmid and *Pik3r1MO* or std-MO were prepared with same concentrations and injected into 1-cell stage embryos.

Imaging at confocal microscope

Injected embryos were kept under standard condition at 28.5 °C and treated with 1-Phenyl-2-thiourea (Sigma-Aldrich) from 24 hours after fertilization. Embryos were manually dechorionated in between 48 and 52 hours after fertilization and selected under Leica fluorescent microscope for RFP vascular and EGFP reporter expression. For confocal imaging, embryos were anesthetized with 4 mg/ml 3-aminobenzoic acid ethyl ester (Tricaine/MS-222) (Sigma-Aldrich) and laterally mounted in 35 mm glass bottom dishes using 1% low-melting agarose containing 0.17 mg/ml tricaine. Confocal images were obtained using either LSM 710 or LSM 880 Airyscan confocal laser microscope (Zeiss) and ZEN 2 software, with ×40 objective for imaging of the trunk and caudal vasculatures. Maximum intensity Z-projections of captured images were generated and analyzed using Fiji (version 2.9.0).

Quantification of caudal vein diameter and vascular bed breadth

The diameter of the embryonic zebrafish caudal vein was measured using Fiji. Three measurements were taken on each embryo (on the left, center, and right side of the image). The degree angle between the head and the neck of the fish was used to determine the developmental stage (Kimmel et al, 1995). Embryos in which the caudal vein was not easily discernible were omitted from the analysis. Comparisons were made using unpaired 2-tailed *t*-test with Welch's correction (using GraphPad Prism 9). SDs are reported as a measure of variability. For knockdown experiments, comparisons were made between uninjected or standard control oligo injected embryos and *pik3r1Mo* injected embryos. For rescue and overexpression experiments, comparisons were done between embryos injected with empty vector together

with *pik3r1Mo* or empty vector only and those injected with *PIK3R1*-expression vectors.

To investigate whether the enlarged caudal vein phenotype in mutant fish resulted from an enlargement of cells constituting the caudal vein or rather from an increase in the number of cells, we measured the distance between neighboring $EGFP^+$ nuclei (for plasmid-injected fish) or between one nucleus and its neighboring ones (for Mo-injected fish), as previously described by Bornhorst et al (2019). Measurements were done using the Imaris software.

Zebrafish immunofluorescence

Injected zebrafish embryos were selected to keep only those displaying fluorescent signal in the vasculature and then anesthetized with Tricaine (Sigma-Aldrich) 56 hours after fertilization and fixed in 4% paraformaldehyde overnight at 4 °C. Subsequently, they were washed in PBS with 3% Tween before blocking with 5% of normal goat serum in PBS with 3% Tween for 2 hours, followed by incubation overnight in chicken anti-GFP (1:200, Aves Labs). Embryos were then washed in PBS with 3% Tween and incubated overnight with FITC-conjugated goat anti-chicken (1:200, Aves Labs). Primary and secondary antibodies were diluted in PBS with 3% Tween containing 0.2% Triton X-100, 1% BSA, and 5% normal goat serum. Stained embryos were mounted in SlowFade Gold (Thermo Fisher Scientific) and imaged on LSM 710 (Zeiss). Images were processed with Fiji as mentioned earlier.

Quantification of extravascular space

Detection of the extravascular space was performed on maximum intensity Z-projection images using an in-house developed script on the basis of EBImage (Pau et al, 2010), Reshape (Wickham, 2007), and Raster (Hijmans and van Etten, 2012) scripts, which allowed to circle and assign an identification to each empty space between vessels. The data obtained were manually cleaned from false positives to keep only the values corresponding to empty spaces on the original confocal image. Each empty space was considered as an ellipse. The final value of the total empty area was then calculated as follows:

$$A = \pi ab$$

The value normalized on the total size of the image and the total area occupied by the vascular bed is represented as a ratio and was performed as follows:

$$\text{Area}_{\text{total}} = \text{image area}$$

$$\text{Area}_{\text{empty space}} = \text{sum of all areas calculated on clean data}$$

$$\text{Area}_{\text{to remove}} = \text{Area}_{\text{total}} - \text{Area}_{\text{empty space}}$$

$$\text{Area}_{\text{of interest}} = \text{Area}_{\text{total}} - \text{Area}_{\text{to remove}}$$

$$\text{Ratio} = \frac{\text{Area}_{\text{empty space}}}{\text{Area}_{\text{to remove}}}$$

This analysis was performed on n =5 embryos per condition and was only focused on the area in between the dorsal aorta (excluded) and the caudal vein (included).

Plasmid integration rate analysis

The rate of plasmid integration was determined by counting nuclei with EGFP ($EGFP^+$) expression. We counted nuclei between the dorsal aorta (excluded) and the caudal vein (included). The counting was performed on confocal Z-stack images of the EGFP channel. SDs are reported as measure of variability.

SUPPLEMENTARY REFERENCES

Asakawa K, Suster ML, Mizusawa K, Nagayoshi S, Kotani T, Urasaki A, et al. Genetic dissection of neural circuits by *Tol2* transposon-mediated Gal4 gene and enhancer trapping in zebrafish. Proc Natl Acad Sci USA 2008;105:1255–60.

Bornhorst D, Xia P, Nakajima H, Dingare C, Herzog W, Lecaudey V, et al. Biomechanical signaling within the developing zebrafish heart attunes endocardial growth to myocardial chamber dimensions. Nat Commun 2019;10:1113.

Herwig L, Blum Y, Krudewig A, Ellertsdottir E, Lenard A, Belting HG, et al. Distinct cellular mechanisms of blood vessel Fusion in the zebrafish embryo. Curr Biol 2011;21:1942–8.

Hijmans RJ, van Etten J. raster: Geographic analysis and modeling with raster data. R package version 2.0-12. 2012. http://CRAN.R-project.org/package=raster. (accessed March 18, 2024).

Jin SW, Bein D, Mitchel T, Chen JN, Stainier DY. Cellular and molecular analysis of vascular tube and lumen formation in zebrafish. Development 2005;132:5199–209.

Kimmel CB, Ballard WW, Kimmel SR, Ullmann B, Schilling TF. Stages of embryonic development of the zebrafish. Dev Dyn 1995;203:253–310.

Limaye N, Kangas J, Mendola A, Godfraind C, Schlögel MJ, Helaers R, et al. Somatic activating PIK3CA mutations cause venous malformation. Am J Hum Genet 2015;97:914–21.

Nicoli S, Knyphausen CP, Zhu LJ, Lakshmanan A, Lawson ND. MiR-221 is required for endothelial tip cell behaviors during vascular development. Dev Cell 2012;22:418–29.

Pau G, Fuchs F, Sklyar O, Boutros M, Huber W. EBImage—an R package for image processing with applications to cellular phenotypes. Bioinformatics 2010;26:979–81.

Rödel CJ, Otten C, Donat S, Lourenço M, Fischer D, Kuropka B, et al. Blood flow suppresses vascular anomalies in a zebrafish model of cerebral cavernous malformations. Circ Res 2019;125:e43–54.

Westerfield M. The Zebrafish Book. A Guide for the Laboratory Use of Zebrafish (Danio rerio). 4th Edition. Eugene: University of Oregon Press; 2000.

Westerfield M, Doerry E, Kirkpatrick AE, Driever W, Douglas SA. An on-line database for zebrafish development and genetics research. Semin Cell Dev Biol 1997;8:477–88.

Wickham H. Reshaping Data with the reshape Package. J Stat Softw 2007:21.

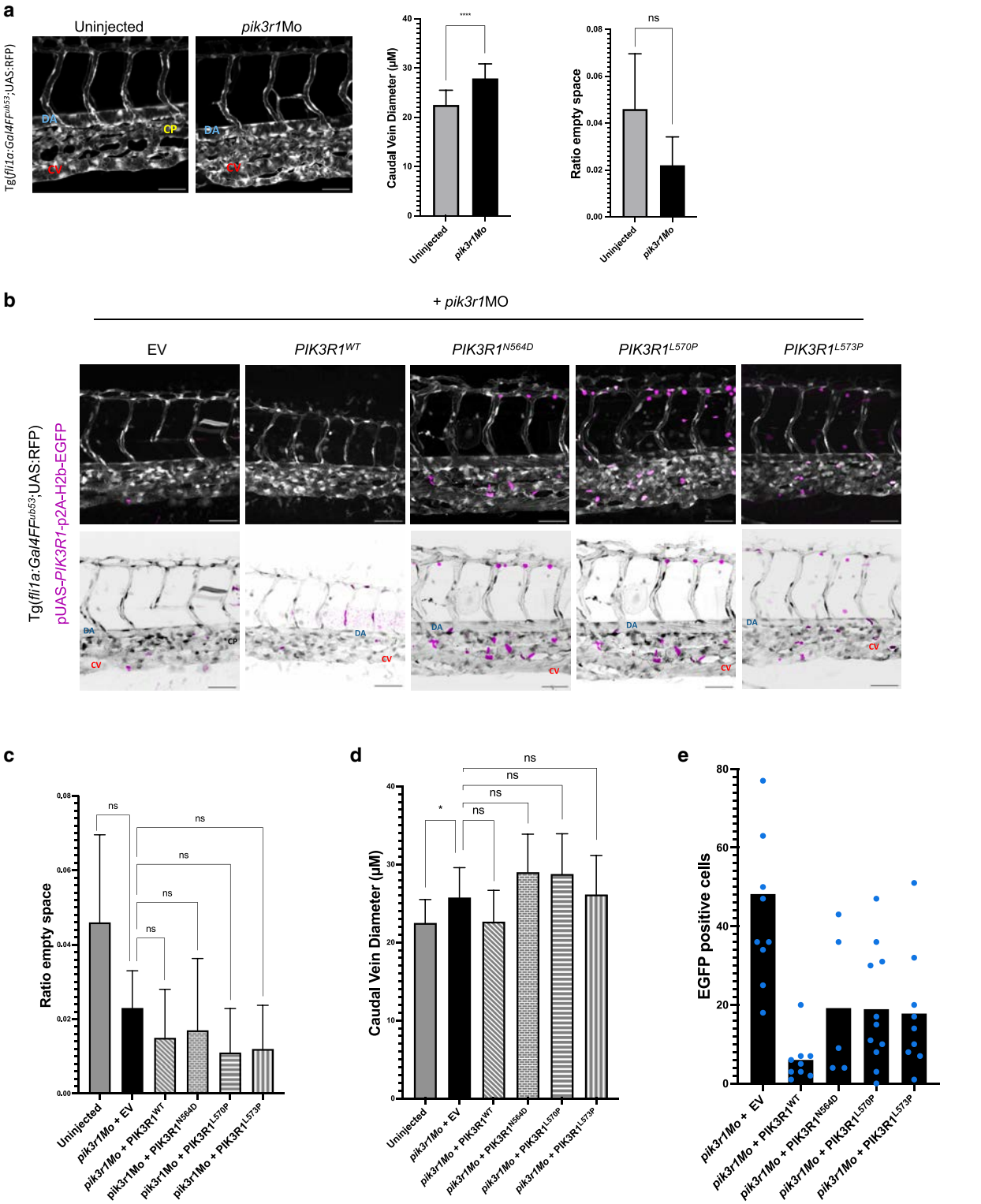

Supplementary Figure S1. Knockdown and rescue of *PIK3R1* expression in Tg(fli1a:Gal4FF^{ub53};UAS:RFP)-positive zebrafish embryos. Normal and inverted images are shown. EGFP^{+} cells (magenta) integrated injected plasmid. CV (red), DA (yellow), CP (blue) are shown. **(a)** Embryos injected with spliced p*ik3r1Mo* and uninjected control. Increased CV diameter but no CP disruption as effect of *PIK3R1* knockdown is shown. **(b)** Embryos injected with p*ik3r1Mo* and pUAS-p2A-H2b-EGFP (EV) or pUAS-*PIK3R1*-p2A-H2b-EGFP (wt/mutated) fail to rescue phenotype given by *pik3r1Mo* knockdown. **(c, d)** Quantification of CV diameter and area in between CV and DA, occupied by capillary bed, shows no difference when knockdown rescued, whether wt or mutant *PIK3R1* expressed. **(e)** Quantification of plasmid integration rate in zebrafish endothelium: number of EGFP^{+} cells found in capillary–venous plexus. Plotted averages normalized on number of embryos per condition. Each blue dot corresponds to 1 embryo. Bar = 50 μM. Error bars are shown as measure of variability and represent the SD.

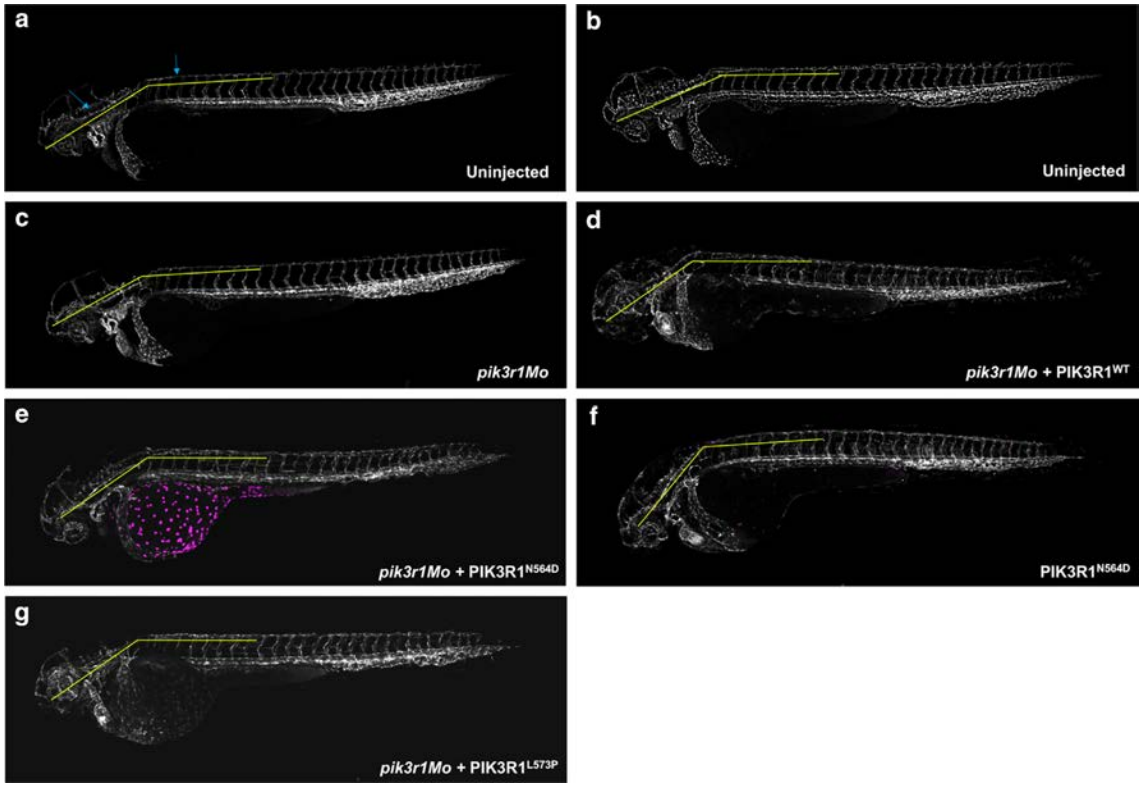

Supplementary Figure S2. Overview (×10) of zebrafish embryos at 48–54 hpf. In yellow, lines indicating the angle between the head and the neck of the fish serve as a reference for determining its developmental stage (Kimmel et al, 1955). Notably, neither morphants nor mutant fish exhibited any indication of developmental delay. hpf, hours post fertilization.

Number of biological replicates: uninjected (n = 19), *pik3r1Mo* (n = 29), EV+ *pik3r1Mo* (n = 10), PIK3R1^{WT} + *pik3r1Mo* (n = 5), PIK3R1^{N564D} (n = 14), PIK3R1^{L570P} + *pik3r1Mo* (n = 14), and PIK3R1^{L573P} + *pik3r1Mo* (n = 9). Embryos in which the CV was not readily distinguishable were discarded. CP, capillary plexus; CV, caudal vein; DA, dorsal aorta; EV, empty vector; ns, not significant; wt, wild type.

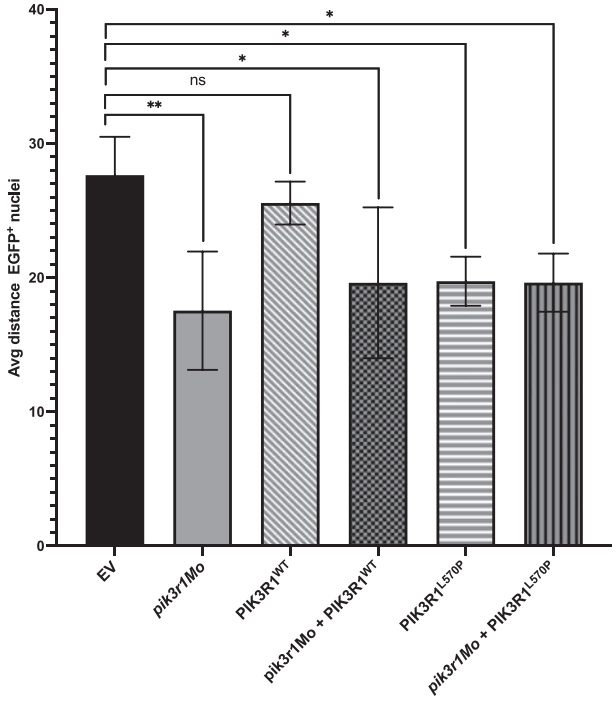

Supplementary Figure S3. Measurement of the average distance between neighboring nuclei to assess cell size. In morphant as well as in mutant fish, cell size was significantly reduced compared with that in EV-injected control fish. This was not the case for overexpressing *PIK3R1*^{WT}, which were not significantly smaller than EV-injected fish. EV, empty vector; ns, not significant.

Supplementary Table S1. Numbers of Embryos Considered for the CV Diameter Analysis

	Condition	Total Number of Embryos	Number Analyzed Embryos	Number of Discarded Embryos	% of Discarded Embryos
	Uninjected	19	19	0	0%
	Pik3r1Mo	33	29	4	12%
	EV	10	10	0	0%
	PIK3R1^{WT}	10	9	1	10%
	PIK3R1^{N564D}	7	4	3	42.8%
	PIK3R1^{L570P}	10	8	2	20%
	PIK3R1^{L573P}	13	9	4	30.7%
+ *pik3r1Mo*	EV	10	10	0	0%
	PIK3R1^{WT}	16	15	1	6.2%
	PIK3R1^{N564D}	21	14	7	33.3%
	PIK3R1^{L570P}	18	14	4	22.2%
	PIK3R1^{L573P}	11	9	2	18.1%

Abbreviations: CV, caudal vein; EV, empty vector; WT, wild type.
Embryos that did not display a clearly distinguishable CV were excluded from the analysis.